Pinning effect on the band gap modulation of crystalline $Be_xZn_{1-x}O$ alloy films grown on $Al_2O_3(0001)$

Dae-Sung Park,[a] James J. Mudd,[a] Marc Walker,[a] Aleksander Krupski,[a] Djelloul Seghier,[a‡] Nessa Fereshteh Saniee,[a] Chel-Jong Choi,[b] Chang-Ju Youn,[b] Sean R. C. McMitchell,[a] and Chris F. McConville*[a]

Received Xth XXXXXXXXXX 20XX, Accepted Xth XXXXXXXXX 20XX

First published on the web Xth XXXXXXXXXX 200X

DOI: 10.1039/b000000x

We have investigated the influence of Be concentration on the microstructure of $Be_xZn_{1-x}O$ ternary films (from x = 0 to 0.77), grown on $Al_2O_3(0001)$ substrates using radio-frequency co-sputtering. With increasing Be concentration, the (0002) X-ray diffraction peak shows a systematic shift from 33.86° to 39.39°, and optical spectroscopy shows a blue-shift of the band gap from 3.24 to beyond 4.62 eV towards the deep UV regime, indicating that Be atoms are incorporated into the host ZnO lattice. During the band gap modulation, structural fluctuations (e.g. phase separation and compositional fluctuation of Be) in the ternary films were observed along with a significant change in the mean grain size. X-ray photoelectron spectroscopy indicates higher concentrations of metallic Be states found in the film with the smaller grain size. Correlation between these two observations indicates that Be segregates to near grain boundaries. A model structure is proposed through simulation, where an increase in grain growth driving force dominates over the Be particle pinning effect. This leads to further coalescence of grains, reactivation of grain growth, and the uniform distribution of Be composition in the $Be_xZn_{1-x}O$ alloy films.

1 Introduction

Wide band-gap oxides have received a great deal of interest due to their potential use in optoelectronic applications, including ultraviolet (UV) laser diodes (LDs), light-emitting diodes (LEDs), high-mobility transistors, and gas sensors.[1–6] The quantum confinement effect (QCE) and the fractional quantum Hall effect (FQHE) are phenomena that have been observed in well-designed oxide heterostructures and can add to the wealth of potential applications.[7] In order to design such quantum structures, it is essential to understand the band-gap engineering of oxides and the nature of oxide-based heterointerfaces. In addition, various charge states can occur at such surfaces and interfaces (either charge accumulation or depletion), as a result of the surface termination, the formation of surface defects (e.g. oxygen vacancies or cation interstitials), the presence of unintentional impurities (e.g. hydrogen, H_i) or other chemisorbed species.[8–10] ZnO-based materials have many applications and exhibit many interesting physical and electronic properties, including a large exciton binding energy ($\approx$ 60 meV) at room temperature, and high transparency in both ultra-violet (UV) and visible spectral ranges.[11] In a wider band-gap engineering process of ZnO-based materials, A. Ohtomo *et al.*[12] first proposed that the band gap energy (E_g) of $Zn_{1-x}Mg_xO$ could be tuned from 3.3 (ZnO) to 7.8 eV (MgO) by substitution of Mg into Zn lattice sites in the wurtzite structure. The alloying process, however, was limited to $x \leq 0.36$ due to a structural transition from the ZnO hexagonal phase to the rocksalt phase of MgO at high concentrations. Ryu *et al.*[13] suggested that the E_g could be fully modulated by alloying with BeO (E_g = 10.6 eV) without a structural phase transition due to the two materials having the same hexagonal symmetry. Subsequently, a $Be_xZn_{1-x}O$-based multi-quantum-well structure was designed by periodically stacking ZnO wells with $Be_{0.2}Zn_{0.8}O$ barriers, resulting in UV light emission generated from a conventional LED structure.[5] After this demonstration, Klingshirn *et al.*[14] suggested that one possible explanation of compositional fluctuations and local segregation was diffusion of Be to the ZnO interfaces in the quantum well device structures. Therefore, understanding the growth mechanisms of $Be_xZn_{1-x}O$ films on highly-mismatched substrates is key to improving device performance. In previous studies, growth of $Be_xZn_{1-x}O$ ternary thin films using various growth methods[15–18] resulted in poor quality single crystals due to the tetrahedral ionic radius of Be^{2+} (0.27Å) being much smaller than that of Zn^{2+} (0.60Å). This size difference can lead to a change in crystal space group from hexagonal ($P6_3mc$) to other crystal symmetries, i.e. orthorhombic ($Pmn2_1$ or $Pna2_1$) or zinc-blende ($F\bar{4}3m$).[19] Also, a miscibility gap the $Be_xZn_{1-x}O$ alloy system can lead to ther-

[a] *Department of Physics, University of Warwick, Coventry CV4 7AL, United Kingdom. Fax: +44-(0)24-7615-0897; Tel: +44-(0)24-7652-4236; E-mail: c.f.mcconville@warwick.ac.uk*

[b] *School of Semiconductor and Chemical engineering, Chonbuk National University, Jeonju 561-756, South Korea.*

‡ *Present address: Science institute, University of Iceland, Dunhaga 3, IS-107 Reykjavik, Iceland.*

modynamic instabilities such as compositional fluctuations or phase segregation.[20] Finally, considerable strain arises from the lattice mismatch between film and substrate. The interface normally favors a three-dimensional (3D) growth mode, resulting in a columnar structure, mixed growth orientations, and a rough surface morphology.[21,22] In this manuscript the influence of Be concentration on grain growth in crystalline $Be_xZn_{1-x}O$ thin films (from x = 0 to 0.77) has been investigated. It was found that a systematic change of the lattice parameter and optical band gap (E_g) occurs with increasing Be concentration. A non-uniform distribution of Be in the films was also observed for compositions ranging from x = 0.16 to 0.41. A particle pinning model has been developed to interpret the compositional fluctuations and segregation of Be, following coalescence of the smaller-sized grains in terms of grain boundary movement as a function of Be concentration.

2 Experimental details

$Be_xZn_{1-x}O$ alloy ($0 \leq x \leq 0.77$) thin films of thickness $\approx$ 200 nm were prepared on c-axis Al_2O_3 substrates in a partial pressure (P_{O2}) of 2×10^{-3} mbar at a growth temperature of 400°C using the radio-frequency (RF = 13.56 MHz) magnetron co-sputtering (base pressure: 1.6×10^{-8} mbar). In order to vary the Be concentration in the films, the RF power to the Be metal target (99.9 %) was adjusted from 0 to 80 W, while the RF power of the ZnO ceramic target (99.999 %) was fixed at 100 W. Films were prepared with almost constant thickness by controlling the deposition time under fixed conditions. Prior to film growth, both ZnO and Be targets were sputtered in the vacuum chamber using a RF power of 50 W in 30 min to remove target surface contaminants.

The structural and optical properties of the films were evaluated by X-ray diffraction (XRD; λ = 1.5418 Å) and UV-visible spectroscopy measurements. Tapping mode atomic force microscopy (AFM) was used to observe the surface morphologies of the films. To determine the surface electronic structure and chemical state of the films as a function of Be composition, X-ray photoelectron spectroscopy (XPS) was performed in ultra-high vacuum (UHV) using an Omicron SPHERA hemisphere analyzer and monochromatic Al K_α source ($h\nu$ = 1486.6 eV). Photo-excited electrons from the film surfaces were collected using a take-off angle of 90°. Surface charging during XPS measurements, resulting from the insulating nature of the samples was compensated for by using a low energy electron flood gun (Omicron CN10). The binding energy (BE) scale was calibrated using the C 1s position (284.5 eV) and the overall energy resolution was 0.6 eV. Elemental composition ratios were extracted including the electron mean free path correction and using Schofield cross sections.[23] Peaks were fitted using a Shirley background and Voigt (convolved Lorentzian-Gaussian) functions.

3 Results and discussion

3.1 Film optical and structural properties

The change in the cut-off wavelength of the transmittance spectra for the $Be_xZn_{1-x}O$ alloy films as a function of Be fraction is shown in Fig. 1(a). The spectral range available (220–850 nm) was insufficient to measure the cut-off for the films with high Be content due to the wider band gap energies. However, there was clearly a continuous shift of the spectra into the deep UV energy region and a high trans-

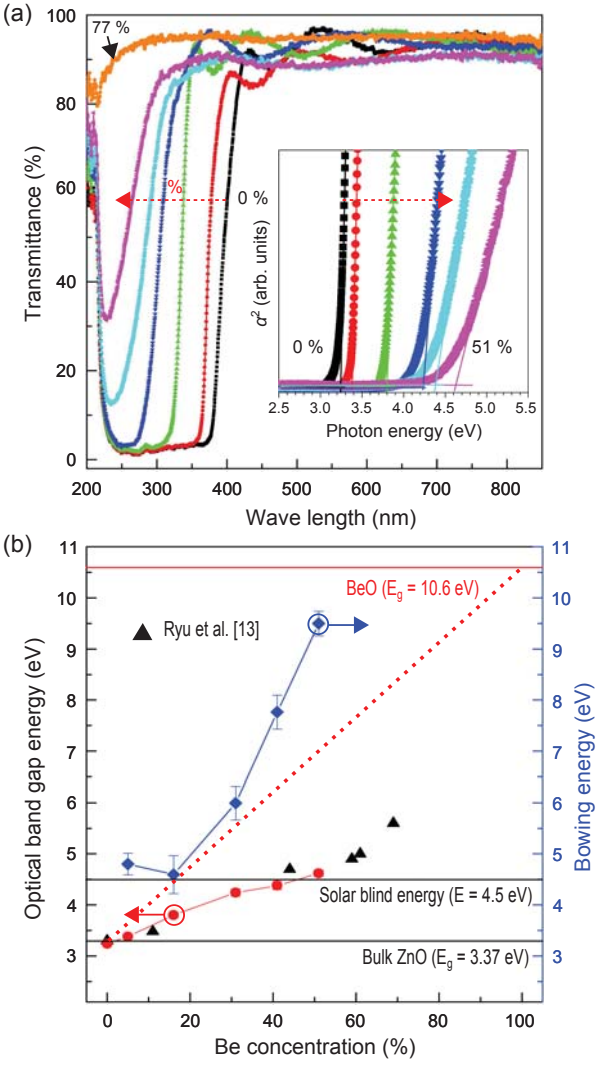

Fig. 1 (a) Transmittance spectra of the $Be_xZn_{1-x}O$ films with an increase in the Be concentration (%), from x = 0 to 0.77, (Inset of (a)) the curve of α^2 *vs* photon energy ($h\nu$) for the films composed by x = 0 to 0.51, and (b) a comparison in band gap energies with the previous report with bowing parameters, b, for the $Be_xZn_{1-x}O$ alloys.

parency of over 85 % as Be concentration increased. Based on these transmittance spectra and excluding reflectivity, the absorption coefficients, α, of the films were evaluated from $T = \mathrm{A}\exp(-\alpha d)$ where T is the transmittance of the film, A is a constant and d is the film thickness. Consequently, by taking a linear extrapolation of the leading edge from the plot of α^2 versus hν, the optical band gap energies in the limit of the spectral region were determined to range from 3.24±0.01 to 4.62±0.06 eV for Be concentrations up to x = 0.51 (see the inset of Fig. 1(a)).[24] Tailing of the absorption edge obtained was found as Be concentration increased. This is commonly associated with a decrease of the crystalline quality.[25,26] As shown in Fig. 1(b), changes in the optical band gap energies, taken from transmittance spectra, exhibited a non-linear dependence on the Be composition due to a large bowing effect. The values of bowing parameters, b, were calculated to be 4.8±0.2, 4.6±0.4, 6.0±0.3, 7.8±0.3 and 9.5±0.2 eV for x = 0.05, 0.16, 0.32, 0.41, and 0.51, respectively. The large b can be attributed to the considerable difference in atomic size and large chemical mismatch between Zn^{2+} and Be^{2+}. Moreover, the larger increase of b at the higher Be composition could be associated with additional band repulsion between the O 2p and the Zn 3d orbitals in the electronic band structure of the Be-rich alloys. The orbital interaction possibly results in an up-shift of valence band and in turn a large band gap reduction.[19,27] The lattice strain effect on the redistribution of the density of states in the hexagonal symmetry of largely mismatched films also requires consideration. Consequently, the optical results confirm that the band gap of ZnO can be tuned by incorporating Be into the host lattice although some structural deterioration should be expected. However, it is noted that the calculated optical values might be overestimated due to spectral merging that allowed the local distribution of Be to effect the optical spectroscopy measurement.

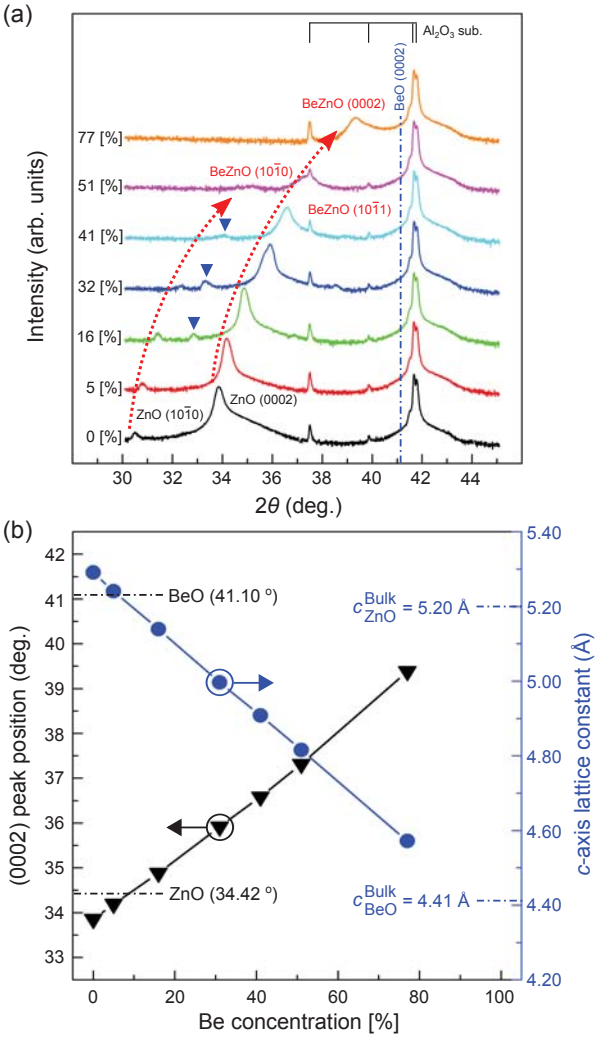

Fig. 2 (a) XRD θ-2θ scans of the $Be_xZn_{1-x}O$ films as a function of Be concentration (%), and abnormal peaks appearing between (10$\bar{1}$0) and (0002) $Be_xZn_{1-x}O$ plane reflections are signified by blue-triangles. (b) (0002) peak positions in 2θ and c-axis lattice parameters as a function of Be content (%).

X-ray diffraction (XRD) patterns of the $Be_xZn_{1-x}O$ thin films grown on Al_2O_3(0001) substrate, taken in the θ-2θ geometry are shown in Fig. 2(a). All films were shown to be preferentially oriented along the c-plane (0001) of wurtzite phase. In addition, (10$\bar{1}$0) and (10$\bar{1}$1) growth orientations were also observed. There was a significant shift in the (0002) diffraction peak position as Be concentration increased. This suggests a structural change from the undoped ZnO structure (33.9°) towards a hexagonal BeO-type structure (41.1°). From this shift, a decrease in c-axis lattice parameter was deduced from 5.23 for to 4.80 Å as shown in Fig. 2(b), confirming the lattice compression required for incorporating Be^{2+} into ZnO. Calculations based on *Vegard*'s law confirmed the Be fraction in the alloy films as x = 0.05, 0.16, 0.31, 0.41, 0.51, and 0.77.[28] This revealed that Be atoms were well-substituted into Zn sites and that the c-axis oriented hexagonal structure was thus primarily maintained in all films. Broadening of the (0002) diffracted peak was also observed as Be composition was gradually increased, suggesting a deterioration of film crystal quality. This is also indicative of a reduction of crystallite size with increasing Be content in the alloy films. It is known that adatom diffusion on a surface to island edges can be kinetically restricted by strain concentration near step edges during island growth. Since the strain-induced energy barrier to adatom movement at the island edge is proportional to lattice mismatch, smaller coherent islands can be formed in higher lattice-mismatch system.[29] Substantial elastic strain energy generated from the lattice mismatch between the $Be_xZn_{1-x}O$ films and the substrate would be further increased with the addition of more Be. This is due to

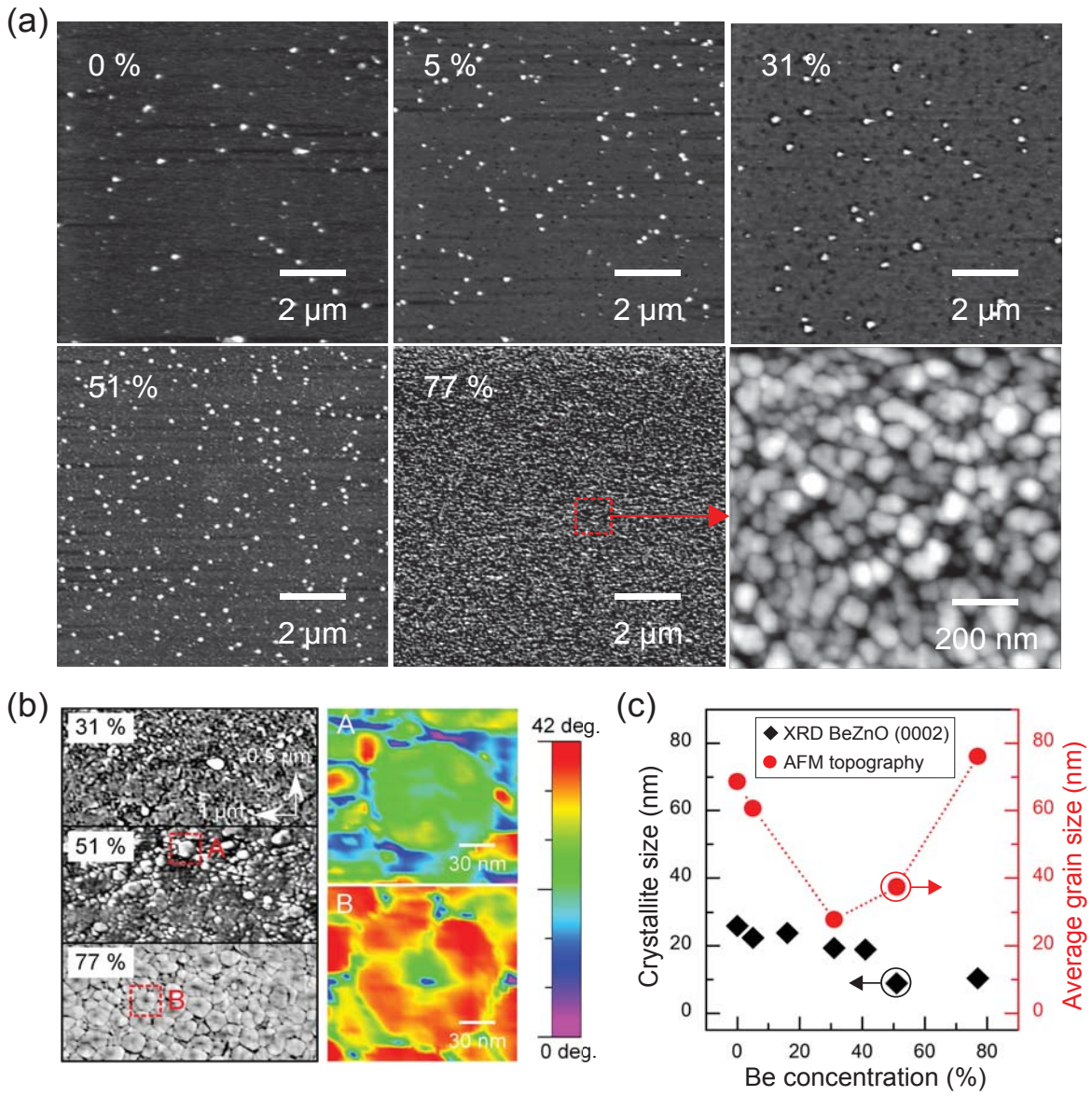

Fig. 3 (a) AFM topography ($10\times10\ \mu m^2$) images of the $Be_xZn_{1-x}O$ films for x = 0, 0.05, 0.31, 0.51, and 0.77, and the ($1\times1\ \mu m^2$) image of the $Be_{0.77}Zn_{0.23}O$ film. (b) Phase ($1\times1\ \mu m^2$) images of the selected $Be_xZn_{1-x}O$ films composed by Be concentration (%), x = 0.31, 0.51, and 0.77, magnified spectrum images (right-top and -bottom) for selected arears -A and -B (x = 0.51 and 0.77), respectively. (c) The profile of crystallite size (based on FWHM values of the (0002) XRD diffraction peaks for the films) and average grain sizes (AFM) as a function of Be concentration (%).

the smaller atomic size of Be and causes smaller crystallites as the excess strain relaxed. Hence, large lattice mismatch (more than 18 %) at the $Be_xZn_{1-x}O$ film/substrate interface is assumed to initiate a three-dimensional (3D) grain growth to minimize the total energy configuration (strain energy + surface energy). This lead to the formation of smaller crystallites and misaligned (tilted/twisted) lattice domains with random orientations.[30,31] As a result, these growth features with smaller grains were induced by the incorporation of smaller Be into the host and the following increase in lattice mismatch strain. Furthermore, since grain growth in films is driven by a reduction of total energy at grain boundaries, the grain boundary migration during film grain growth could play a crucial role in the formation of crystalline $Be_xZn_{1-x}O$ films. This point will be discussed in more detail later. In the range from Be concentration, x = 0.16 to 0.41, asymmetrically split (0002)

peaks and extra peaks between the $(10\bar{1}0)$ and (0002) orientations were clearly observed (Fig. 2(a)). These two distinct peaks shifted towards each other as Be concentration increased and merged to form a single peak at a concentration of $x = 0.51$. The peak then reduced in intensity and, disappeared at the highest Be concentration of $x = 0.77$, where only an hexagonal (0002) peak was seen. Structural fluctuations may be attributed to a non-uniform distribution of Be atoms and a higher level of lattice stress from grain boundaries and the substrate interface during film growth. In previous theoretical studies, phase separation in the $Be_xZn_{1-x}O$ alloy system was also expected due to the large enthalpy of alloy formation arising from the large mismatch between ZnO and BeO.[20,32]

3.2 Film surface morphology and chemical composition

AFM topography images ($1\times1\ \mu m^2$) of the $Be_xZn_{1-x}O$ films grown on *c*-axis oriented Al_2O_3 substrates are shown in Fig. 3(a). The images indicate that all films exhibited a granular microstructure corresponding to a three-dimensional (3D) columnar growth mode. Grain size varied and were randomly distributed on the film surfaces up to $x = 0.51$. For $x = 0.77$, a smaller grain size became dominant as shown in the $1\times1\ \mu m^2$ scan of the $Be_{0.77}Zn_{0.23}O$ film (right-bottom image in Figure 3a). The distribution of grain sizes on the film surfaces was consistent with XRD measurements, which indicated a coexistence of different growth orientations and a broadening of the (0002) diffraction peak.[31] The average grain size for the films were found to decrease from ≈ 68.6 nm for $x = 0$ to ≈ 27.8 nm at x = 0.31. An increase of grain size followed at higher values of x to ≈ 76.0 nm at $x = 0.77$. It should be noted that the average grain size obtained from AFM analysis differed from that obtained from XRD using the *Debye-Scherrer* formula, as depicted in Fig. 3(c).[33] Further insight into this can be obtained by analysis of the AFM phase images (Fig. 3(b)). It was found that the average grain size appeared larger due to a set of fine-grains along grain boundaries combining as Be concentration increased from $x = 0.31$ to 0.77. This is shown by spectral images of the selected grains (A and B). This revealed that the formation of the larger grains was a consequence of fine grain coarsening at the grain boundary junctions.

The XPS spectra of Be 1*s* and Zn 3*p* core-levels for the $Be_xZn_{1-x}O$ films are shown in Fig. 4(a).A spin-orbit split Zn 3*p* doublet was observed at approximately 89 eV.[34] The Zn 3*p* core-level peak showed broadening and a shift to the higher BE region with increasing Be concentration. This is attributed to a distribution of Zn ions in different net-charge states in the wurtzite alloy coordination, the presence of a variety of surface species (e.g. surface hydroxylation on polar surfaces: Zn-O-H), and the increased of number of Zn ions in defect states.[35,36] These imply an increased surface area to volume ratio on decreasing the crystallite size and a non-stoichiometric wurtzite environment as Be concentration rises.

As seen in Fig. 4(b), the XPS spectrum for the undoped ZnO film showed a broad feature (≈ 100 to ≈ 120 eV) originating from screening effects of photo-excited electrons from surface plasmon excitation and inelastic collision processes (e.g. electron-electron and electron-phonon scatterings). This implies that the film surface possessed free-electron carriers due to native defects/unintentional impurities (e.g. V_O, Zn_i and H_i) as is typical in undoped ZnO. It could have also contributed to a surface band bending effect.[8,9,37] The relative intensity of the plasmon peak decreased continuously as Be concentration increased. This revealed both a reduction of free carriers and the deterioration of crystallinity in terms of the number of photo-excited electrons with a relatively long-pass distance on the film surfaces. So, the surface plasmon effects on the $Be_xZn_{1-x}O$ film surfaces at high Be content in Be 1*s* core-level was negligible, allowing the Be 1*s* core-level to be fitted by two components at BEs of $\approx$111 and $\approx$ 114 eV, respectively (denoted in Fig. 4(b)). Those two distinct components were associated with metallic Be (Be_M) and Be-O bond (Be_O) states on the surface.[38,39] The Be_O peak intensity increased continuously, again suggesting that Be was well incorporated into the host lattice. This is consistent with the above XRD and optical spectroscopy measurement results.

The highest ratio of Be_M to Be_O was observed at a Be con-

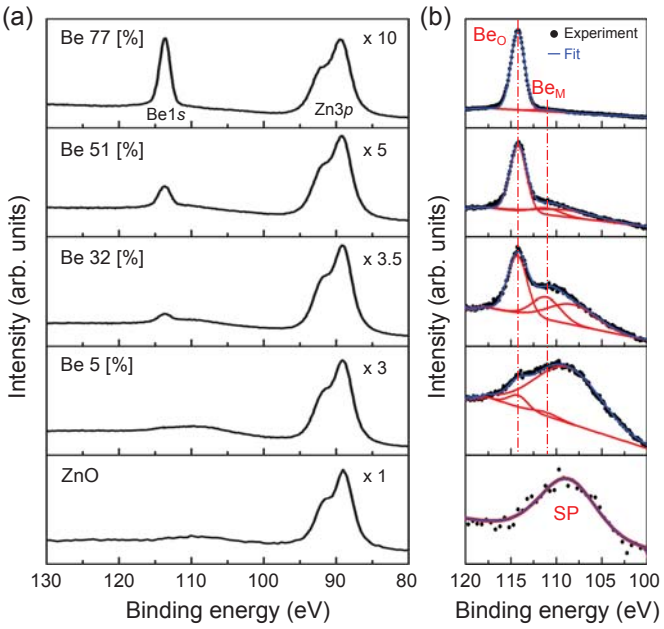

Fig. 4 (a) Be 1*s* and Zn 3*p* XPS spectra of the $Be_xZn_{1-x}O$ alloys as Be fraction, *x*, increases. (b) Experimental Be 1*s* core level spectra for all films are fitted using Be-O bonding (Be_O), metallic Be (Be_M), and surface plasmon (SP) components using a Shirley background and Voigt line shapes (solid lines).

Table 1 Parameters (binding energy, Lorentzian percentage of the Voigt line shape (*L*), and full width at half maximum (FWHM)) of Be 1*s* core level fitting, quantification values (%) of Be-O bonding (Be_O) and metallic Be bonding (Be_M), and the ratio of Be_O/(Zn+Be_O for the $Be_xZn_{1-x}O$ alloy films as a function of Be concentration obtained from the XPS spectra (Al Kα hν = 1486.6 eV). The quantification analysis of atomic compositions (O, Zn, and Be) for all films was determined from the areas of the O 1*s*, Zn 3*s*, and Be 1*s*.

Sample	Bonding	Binding energy (eV)	*L* (%)	FWHM (eV)	Relative Percentage (%)	Be_O/(Zn+Be_O)
Be 5 %	Be_O	114.2	8	2.2	4.3	0.1
	Be_M	111.2	8	3.2	1.8	
Be 31 %	Be_O	114.4	8	2.3	17.8	0.4
	Be_M	111.2	8	3.7	11.2	
Be 51 %	Be_O	114.2	8	2.1	31.8	0.6
	Be_M	111.0	8	3.7	4.5	
Be 77 %	Be_O	114.3	8	1.8	44.8	0.8
	Be_M	111.1	8	3.0	1.6	

centration of x = 0.31. Then, a continuous decrease of the ratio was observed with further addition of Be up to x = 0.77. All fitting parameters and the relative percentages of Be_M and Be_O for the Be 1*s* core level spectra found by evaluating the O 1*s*, Zn 3*s*, and Be 1*s* core-levels for all $Be_xZn_{1-x}O$ films are presented in Table 1. The surface Be_O composition relative to the Zn composition (Be_O/(Zn+Be_O)) was higher compared to the film bulk. A possible explanation is that this is caused by a surface segregation process through the higher removal of surface Zn atoms to minimize surface energy.[35,40,41]

3.3 Particle pinning model and discussion

A possible mechanism for this type of grain growth of crystalline $Be_xZn_{1-x}O$ on Al_2O_3 substrates can be described by a model first suggested by Zener *et al.*. The model describes secondary phase particles, in this case metallic Be, at grain boundaries pinning the boundaries and restricting grain wall motion. This grain boundary drag caused by Be particles at grain boundaries would lead to the formation of smaller grains during growth as illustrated in Fig. 5(a). It should be noted that the original Zener *et al.* model was used to describe a three dimensional array of grains and, therefore, the model below has been modified to account for the planar nature of film growth. It was found that Be concentration in the alloy films significantly affects grain structure and size. It is common in grain growth that the grain size depends on the migration of grain boundaries arising from the difference in grain curvatures (pressure; P_g), which are due to the chemical potential difference ($\Delta\mu$) described by[30,42,43]

$$\Delta\mu = \frac{2\gamma}{D} = P_g, \tag{1}$$

where γ and D are interfacial energy at the boundary and mean grain size, respectively. Here, the matrix grain boundary mobility is interrupted by pinning of solute particles occuping the grain boundary areas.[44] Pinning particles at grain boundaries reduce the Gibbs free energy, retarding the movement of the matrix grain boundaries during growth. A pinning particle of circumference 2π r$\cos\theta_1$ is placed at the grain boundary, as illustrated in Fig. 5(a) where r is the radius of particle. The maximum pinning pressure (P_p) of the particles can be expressed as

$$P_p = \frac{3f}{2\pi r^2} \cdot 2\pi r \cos\theta_1 \gamma \sin\theta_2 \approx \frac{3f\gamma}{2r}, \tag{2}$$

where f is the volume fraction of the particles in the unit area of a random plane. The first term is the mean number of the particles intersecting a unit area of a random plane and the second term is the maximum particle pinning force with a drag angle of $\theta_1 = 45^\circ$ and a surface pulling angle of $\theta_2 = 90^\circ$ at the grain boundary.In the above equation, the two driving pressures counterbalance each other, and the pinned grain size, D_{max}, is approximately determined by

$$D_{max} = \frac{4r}{3f}, \tag{3}$$

Metallic Be particles may favor lower energy sites at grain boundaries rather than in the matrix of the grain, subsequently inhibiting the grain boundary mobility. This results in a reduction of grain size as shown in Fig. 5(b). In a similar case, B. Ingham *et al.* reported that metallic Al atoms at grain boundaries restricted ZnO grain growth in the formation of spinel crystallites as $ZnAl_2O_3$.[45] In this work, AFM and XPS showed that the mean grain size was inversely proportional

to the amount of metallic Be on the film surface. Furthermore, it can be assumed that by increasing Be content in the films, the volume fraction of Be particles at grain boundaries increased. There was, however, an inconsistency in crystallite size and mean grain size measured by XRD and AFM as seen in Fig. 3(c). This discrepancy could be reconciled by considering the change in the Be pinning pressure at grain boundaries with an increase in Be pinning particle size. This would have driven an Ostwald ripening of the Be particles at grain boundary interfaces, resulting in a coarsening of the particles and in turn decreasing the pinning pressure, P_p.[46] When the driving pressure of grain growth was sufficient to overcome pinning pressure of Be particles, movement of the grain boundaries occured to allow coalescence. Interestingly, it appeared that a two-step coalescence process occured at a Be concentration of $x = 0.77$. Initially, fine-sized grains coarsened to concave inward to form an eight-junction grain boundary that minimized interface energy between the grains. Then, a set of these coarsened fine-grains combined in a triple-junction boundary favoring a distinctly shaped grain growth to produce an abnormal grain growth mode. At the same time, Be particles could encounter the lattice matrix grains due to a mass transport driven by the Be concentration gradient. Eventually, Be concentration would become uniformly distributed across the fine grains via the grain boundary junctions leading to reduction in metallic Be states, as shown by XPS.

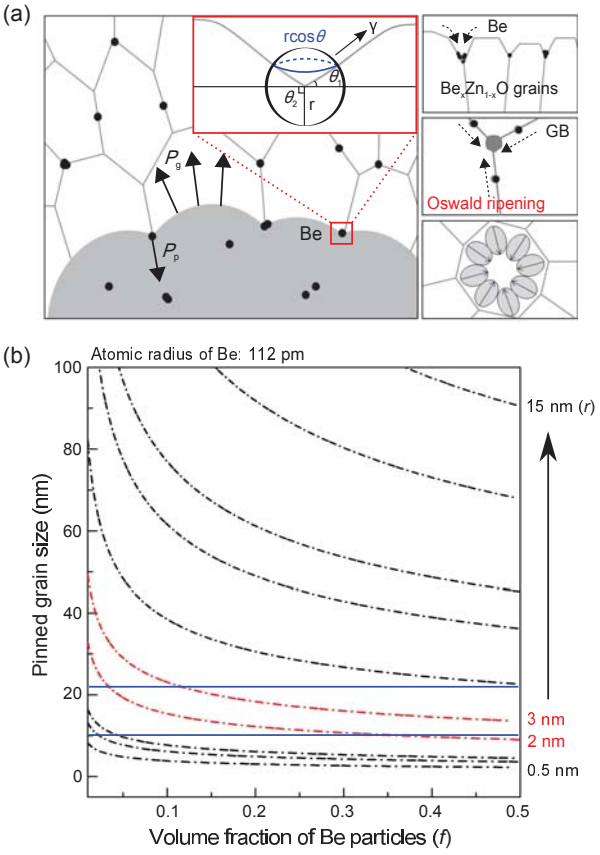

Fig. 5 (a) Schematic diagrams for grain growth model for crystalline $Be_xZn_{1-x}O$ pinned by Be particles,[30] and (b) pinned grain size D_p as a function of volume fraction f of Be pining particles, for values of the Be particle radius, r, from 0.5 to 15 nm. The region between the two solid-blue lines represents the pinned grain size range with Be particle size of 2–3 nm, which is consistent with the experimental results.

The approximate sizes of Be pinning particles depend on the volume fraction of the particles and the pinned grain size as depicted in Fig. 5(b). Zener *et al.* first proposed a model with a random distribution of second phase particles at random boundary intersections, i.e. the volume fraction, f[1], of the particles is represented by a random dispersion in both the planar (2D) and volume (3D) cases.[44] In the model proposed here, since it is most likely that Be pinning particles were located at grain boundaries rather than inthe bulk of the $Be_xZn_{1-x}O$ matrix grains, the model has been modified to require a non-random distribution of Be particles in a 3D system. Hillert *et al.*[47] also suggested an applicable pinning model in which a 3D volume fraction of particles lead to modified parameters, as given by

$$\tilde{D}_{\max} = \frac{3.6r}{3f^{0.33}}, \tag{4}$$

where $\tilde{D}_{\max}$ is the pinned maximum grain size in a 3D system. Using this modification, the simulated plots (denoted by red dot-dashed line in Fig. 5(b)) pinned grain sizes for Be particle size of 2-3 nm are in good agreement with the AFM data. Note that in this approximation of pinned grain sizes several plausible interactions (e.g. Be particle drag, Be solute precipitation, and re-dissolution) between grain boundaries and the Be solute have been considered. Another aspect of this studywas the possible coupling between grain size being restricted by Be particles at grain boundaries and the resulting surface variation on the films which could have played a significant role in the compositional fluctuations of Be and, thus, the grain boundary structures. As the $Be_xZn_{1-x}O$ grain matrix is encountered by Be particles, the surface curvature of the matrix grain would give rise to the local distribution of Be. In addition, an increased grain boundary area would promote an increase in effective surface area (higher surface-to-volume ratio), encouraging surface chemisorptions such as oxygen. This would lead to the formation of charge trapping/scattering centers, and thus potential barriers for charge transport.[48,49] Therefore, the variation in the surface properties during grain growth was a matter of concern as it could cause substantial non-uniformity in film properties and make application of $Be_xZn_{1-x}O$ in quantum structures or, indeed, other heterostructures problematic.

4 Conclusions

Crystalline $Be_xZn_{1-x}O$ films ($0 \leq x \leq 0.77$) have been grown on *c*-axis Al_2O_3 substrates by RF co-sputtering. A band gap modulation of the $Be_xZn_{1-x}O$ films has clearly been confirmed while maintaining a hexagonal crystal structure. A continuous shift in c- parameter of the hexagonal structure was observed from 5.23 for to 4.80 Å, and an optical band gap shift towards the deep UV regions (from 3.24 to over 4.62 eV)was also seen. Variations in grain growth of $Be_xZn_{1-x}O$ films on large-mismatched substrates were observed and showed that the Be concentration in the films affected the distribution of grains in terms of orientation, size, and composition. In order to interpret the variation of grain growth kinetics with change in Be concentration, a modified Zener model that describes metallic Be particles driving a pinning effect on grain boundary motion was employed. It was shown that grain boundary drag from Be pinning particles induced local Be compositional fluctuation leading to smaller grain sizes. Conversely, coalescence of Be pinning particles at grain boundaries, along with increased Be volume fraction, could give rise to a re-enhancement of the grain growth driving force. This could lead to the formation of a coarse-grained array through the development of specific grain boundary junction-types. The grain boundary junctions also act as a channel for uniform distribution of Be within the crystalline $Be_xZn_{1-x}O$ ternary alloy films.

Acknowledgments

The authors are grateful for technical support from R. I. Johnston and useful discussion with Dr. T. P. A. Hase at the University of Warwick, UK. Access to equipments used in this study was provided through the Science City Research Alliance (SCRA) with capital equipment funding from Advantage West Midlands (AWM) and the European Research and Development Fund (ERDF).

References

1 H. Long, G. Fang, S. Li, X. Mo, H. Wang, H. Huang, Q. Jiang, J. Wang and X. Zhao, *Elec. Dev. Lett., IEEE*, 2011, **32**, 54 –56.
2 S. Chu, G. Wang, W. Zhou, Y. Lin, L. Chernyak, J. Zhao, J. Kong, L. Li, J. Ren and J. Liu, *Nat. Nanotech.*, 2011, **6**, 506–510.
3 Y. W. Heo, Y. W. Kwon, Y. Li, S. J. Pearton and D. P. Norton, *Appl. Phys. Lett.*, 2004, **84**, 3474–3476.
4 K. Nakahara, S. Akasaka, H. Yuji, K. Tamura, T. Fujii, Y. Nishimoto, D. Takamizu, A. Sasaki, T. Tanabe, H. Takasu, H. Amaike, T. Onuma, S. F. Chichibu, A. Tsukazaki, A. Ohtomo and M. Kawasaki, *Appl. Phys. Lett.*, 2010, **97**, 013501.
5 Y. R. Ryu, T. S. Lee, J. A. Lubguban, H. W. White, B. J. Kim, Y. S. Park and C. J. Youn, *Appl. Phys. Lett.*, 2006, **88**, 241108.
6 A. Tsukazaki, A. Ohtomo, T. Kita, Y. Ohno, H. Ohno and M. Kawasaki, *Science*, 2007, **315**, 1388–1391.
7 A. Tsukazaki, S. Akasaka, K. Nakahara, Y. Ohno, H. Ohno, D. Maryenko, A. Ohtomo and M. Kawasaki, *Nat. Mater.*, 2010, **9**, 889.
8 P. D. C. King, T. D. Veal, A. Schleife, J. Z. niga Pérez, B. Martel, P. H. Jefferson, F. Fuchs, V. M. noz Sanjosé, F. Bechstedt and C. F. McConville, *Phys. Rev. B*, 2009, **79**, 205205.
9 M. W. Allen, C. H. Swartz, T. H. Myers, T. D. Veal, C. F. McConville and S. M. Durbin, *Phys. Rev. B*, 2010, **81**, 075211.
10 A. Janotti and C. G. V. de Walle, *Rep. Prog. Phys.*, 2009, **72**, 126501.
11 R. F. Service, *Science*, 1997, **276**, 895.
12 A. Ohtomo, M. Kawasaki, T. Koida, K. Masubuchi, H. Koinuma, Y. Sakurai, Y. Yoshida, T. Yasuda and Y. Segawa, *Appl. Phys. Lett.*, 1998, **72**, 2466–2468.
13 Y. R. Ryu, T. S. Lee, J. A. Lubguban, A. B. Corman, H. W. White, J. H. Leem, M. S. Han, Y. S. Park, C. J. Youn and W. J. Kim, *Appl. Phys. Lett.*, 2006, **88**, 052103.
14 C. Klingshirn, J. Fallert, H. Z. and H. Kalt, *Appl. Phys. Lett.*, 2007, **91**, 126101.
15 C. Yang, X. M. Li, Y. F. Gu, W. D. Yu, X. D. Gao and Y. W. Zhang, *Appl. Phys. Lett.*, 2008, **93**, 112114.
16 J. M. Khoshman, D. C. Ingram and M. E. Kordesch, *Appl. Phys. Lett.*, 2008, **92**, 091902.
17 W. J. Kim, J. H. Leem, M. S. Han, I. W. Park, Y. R. Ryu and T. S. Lee, *J. Appl. Phys.*, 2006, **99**, 096104.
18 M. Han, J. Kim, T. Jeong, J. Park, C. Youn, J. Leem and Y. Ryu, *J. Cryst. Growth*, 2007, **303**, 506 – 509.
19 L. Dong and S. P. Alpay, *Phys. Rev. B*, 2011, **84**, 035315.
20 C. K. Gan, X. F. Fan and J.-L. Kuo, *Comp. Mater. Sci.*, 2010, **49**, S29 – S31.
21 I. W. Kim and K. M. Lee, *Nanotechnology*, 2008, **19**, 355709.
22 S. I. Park, T. S. Cho, S. J. Doh, J. L. Lee and H. J. Jung, *Appl. Phys. Lett.*, 2000, **77**, 349–351.
23 J. Scofield, *j. electron spectrosc. relat. phenom.*, 1976, **8**, 129 – 137.
24 J. I. Panlove, *Optical Processes in Semiconductors*, Dover Publications Inc., 1971.
25 A. Meeder, D. F. Marrón, A. Rumberg, M. C. Lux-Steiner, V. Chu and J. P. Conde, *J. Appl. Phys.*, 2002, **92**, 3016–3020.
26 R. C. Rai, M. Guminiak, S. Wilser, B. Cai and M. L. Nakarmi, *J. Appl. Phys.*, 2012, **111**, 073511.
27 H. L. Shi and Y. Duan, *Eur. Phys. J. B*, 2008, **66**, 439–444.
28 A. R. Denton and N. W. Ashcroft, *Phys. Rev. A*, 1991, **43**, 3161–3164.
29 Y. Chen and J. Washburn, *Phys. Rev. Lett.*, 1996, **77**, 4046–4049.
30 M. Ohring, *Materials Sience of Thin Films*, Academic Press, 2002.
31 C. V. Thompson and R. Carel, *J. Mech. Phys. Solids*, 1996, **44**, 657 – 673.
32 X. F. Fan, Z. Zhu, Y.-S. Ong, Y. M. Lu, Z. X. Shen and J.-L. Kuo, *Appl. Phys. Lett.*, 2007, **91**, 121121.
33 W. Dang, Y. Fu, J. Luo, A. Flewitt and W. Milne, *Superlattices and Microstructures*, 2007, **42**, 89 – 93.
34 S. B. Amor, M. Jacquet, P. Fioux and M. Nardin, *Appl. Surf. Sci.*, 2009, **255**, 5052 – 5061.
35 M. W. Allen, D. Y. Zemlyanov, G. I. N. Waterhouse, J. B. Metson, T. D. Veal, C. F. McConville and S. M. Durbin, *Appl. Phys. Lett.*, 2011, **98**, 101906.
36 Y. Y. Tay, S. Li, C. Q. Sun and P. Chen, *Appl. Phys. Lett.*, 2006, **88**, 173118.
37 P. D. C. King, T. D. Veal, D. J. Payne, A. Bourlange, R. G. Egdell and C. F. McConville, *Phys. Rev. Lett.*, 2008, **101**, 116808.
38 A. Wiltner and C. Linsmeier, *New J. Phys.*, 2006, **8**, 181.
39 C. Linsmeier and J. Wanner, *Surf. Sci.*, 2000, **454**, 305 – 309.
40 D. P. Woodruff and T. A. Delchar, *Modern Techniques of Surface Sciene-Second Edition*, Cambridge University Press, 1944.
41 G. Kresse, O. Dulub and U. Diebold, *Phys. Rev. B*, 2003, **68**, 245409.
42 K. E. E. David A, Porter and M. Y. Sherif, *Phase Transformations in*

Metals and Alloys, CRC Press, 1984.
43 J. E. Burke and D. Turnbull, *Prog. Metal Phys.*, 1952, **3**, 220.
44 C. Zener, *Trans. AIME*, 1948, **175**, 15.
45 B. Ingham, R. Linklater and T. Kemmitt, *J. Phys. Chem. C*, 2011, **115**, 21034–21040.
46 J. M. E. Harper, J. C. Cabral, P. C. Andricacos, L. Gignac, I. C. Noyan, K. P. Rodbell and C. K. Hu, *J. Appl. Phys.*, 1999, **86**, 2516–2525.
47 M. Hillert, *Acta Metallurgica*, 1965, **13**, 227 – 238.
48 W.-R. Liu, W. F. Hsieh, C.-H. Hsu, K. S. Liang and F. S.-S. Chien, *J. Appl. Cryst.*, 2007, **40**, 924.
49 S. M. Hearne, E. Trajkov, D. N. Jamieson, J. E. Butler and S. Prawer, *J. Appl. Phys.*, 2006, **99**, 113703.